Results in Physics 50 (2023) 106548

Contents lists available at ScienceDirect

Results in Physics

journal homepage: www.elsevier.com/locate/rinp

High bandwidth performance of multimode graded-index microstructured polymer optical fibers

Svetislav Savović [a,b], Ana Simović [a], Branko Drljača [c], Milan S. Kovačević [a], Ljubica Kuzmanović [a], Miloš Ivanović [a], Alexandar Djordjevich [b], Konstantions Aidinis [d,e], Daniele Tosi [f], Rui Min [g,*]

[a] Faculty of Science, University of Kragujevac, R. Domanovića 12, 34000 Kragujevac, Serbia
[b] Department of Mechanical Engineering, City University of Hong Kong, 83 Tat Chee Avenue, Hong Kong, China
[c] Faculty of Sciences, University of Priština in Kosovska Mitrovica, Lole Ribara 29, 38220 Kosovska Mitrovica, Serbia
[d] Department of Electrical Engineering, Ajman University, P.O. Box 346, Ajman, United Arab Emirates
[e] Center of Medical and Bio-allied Health Sciences Research, Ajman University, Ajman P.O. Box 346, United Arab Emirates
[f] School of Engineering, Nazarbayev University, Astana, Kazakhstan
[g] Center for Cognition and Neuroergonomics, State Key Laboratory of Cognitive Neuroscience and Learning, Beijing Normal University at Zhuhai, Zhuhai 519087, China

A B S T R A C T

The investigation of the bandwidth in multimode graded-index microstructured polymer optical fiber (GI mPOF) with a solid core is proposed using a modal diffusion approach. For a variety of launch radial offsets of multimode GI mPOF, bandwidth is reported by numerically solving the time-dependent power flow equation (TD PFE) using the explicit finite difference method (EFDM) and physics-informed neural networks (PINN). The decline in bandwidth with fiber length becomes slower at fiber lengths close to the coupling length L_c at which an equilibrium mode distribution (EMD) is attained, showing that mode coupling enhances bandwidth at longer fiber lengths. As fiber length is increased, bandwidth approaches complete independence from radial offset, suggesting the steady-state distribution (SSD) has been reached. We compare multimode GI mPOF performance in terms of bandwidth with that of traditional multimode GI POFs made of the same material. Higher bandwidth performance and quicker bandwidth improvement are displayed by the GI mPOF. To enhance fiber performance in GI mPOF links, such a fiber characterization can be used.

Introduction

High-speed short-range signal transmission via POF has drawn a lot more attention in recent years [1–2]. POF's benefits of a large core, a simple connection, and a diversity of materials [3–16] may offer a cost-effective option for the in-home network. Up until now, POF has most typically been produced using Polymethyl-methacrylate (PMMA) [17]. POF can generally be divided into three types: single-mode [18], few-mode [12], and multimode [19] fibers. The two refractive index (RI) distributions that are most frequently used to create POFs are step-index (SI) [20] and GI [21] distributions. The RI distribution of GI multimode POF continually lowers from the core axis to the cladding. Using this RI distribution, intermodal dispersion can be reduced, the POF's bandwidth can be improved, and transmission distance may be raised. However, in order to manufacture GI POF, advanced doping techniques are required.

The versatility in designing the optical fiber is greatly increased by the microstructure of microstructured optical fiber (MOFs). Many excellent MOF properties [22], including birefringence [23], light dispersion [24], supercontinuum light [25], and wavelength conversion [26], have been investigated by modifying the microstructure. The fabrication of multimode mPOF was first reported by Eijkelenborg et al. in 2001 [27], and afterwards, mPOF garnered research interest for its various uses [28–29]. An optical fiber called a multimode mPOF is made to simultaneously guide numerous light modes. It has a core region surrounded by cladding, and the core and/or cladding region's periodic arrays of air holes give it its distinctive structure. Thus, an mPOF can have its core and/or cladding layer modified by changing the placement and/or size (d) of air holes (Fig. 1). In Fig. 1, a mPOF that mimics a GI optical fiber features a core with different-sized air-holes. Instead of requiring complex doping methods, GI mPOF has the advantage of being more adjustable when it comes to altering the air-hole diameters d and pitch Λ. Additionally, research has shown that GI mPOF has a wider bandwidth than conventional multimode GI POF [30,31]. Numerous industries, including telecommunications, sensing, and imaging in medicine, use multimode GI and SI mPOFs. They are appropriate for

* Corresponding author.
E-mail address: rumi@alumni.upv.es (R. Min).

https://doi.org/10.1016/j.rinp.2023.106548
Received 23 March 2023; Received in revised form 7 May 2023; Accepted 11 May 2023
Available online 22 May 2023

high-power applications due to their large mode areas and ability to transmit high-power lasers. Due to their high sensitivity to variations in the refractive index of the surrounding medium, they are also beneficial for sensing applications.

The PFE is used to characterize transmission performance of different types of conventional multimode optical fibers [31–35] and is thus the most promising tool for modeling multimode MOFs. Since other two alternative approaches, wave optics or geometrical optics, are not able to offer an efficient and accurate modeling tool for transmission characteristics of multimode optical fibers (including MOFs), the importance of the approach used in this work is obvious. A very good efficiency and accuracy of the method used in this work has already been demonstrated in modeling bandwidth of conventional multimode GI POF [35]. Following this route, the bandwidth in GI mPOF for a various launch radial offsets is determined in this paper, to the best of our knowledge for the first time, by numerically solving the TD PFE. These theoretically obtained results for multimode GI mPOF bandwidth are contrasted with previously reported bandwidth for conventional multimode GI POFs [35]. The results reported in this study can be useful for various MOFs applications [36–39].

GI mPOF design

Fig. 1 shows a GI mPOF that was considered in this investigation. Six air-hole rings, numbered rings 1, 2,…, 6, make up the GI mPOF. The fiber material is a PMMA, and the air holes are held in place by a triangular lattice with a pitch of Λ. The air-hole diameter in rings 5 and 6 is the same as the air-hole diameter in ring 4 ($d_4 = d_5 = d_6$). The TI PFE was used to simulate this system.

TD PFE for GI optical fibers

The RI profile of GI optical fiber may be expressed as:

$$n(r,\lambda) = \left\{ \begin{array}{ll} n_{co}(\lambda)\left[1 - 2\Delta(\lambda)\left(\frac{r}{a}\right)^g\right]^{1/2} & (0 \leqslant r \leqslant a) \\ n_{co}(\lambda)[1-2\Delta(\lambda)]^{1/2} = n_{cl}(\lambda) & (r > a) \end{array} \right\} \tag{1}$$

where $n_{co}(\lambda)$ is the maximum RI of the core (measured at the fiber axis), $n_{cl}(\lambda)$ is the RI of the cladding, $\Delta(\lambda) = (n_{co}(\lambda) - n_{cl}(\lambda))/n_{co}(\lambda)$ is the relative RI difference, g is the core index exponent and a is the core radius (Fig. 1). The wavelength λ of the source determines the optimum value of the core RI exponent g to get the maximum bandwidth.

For multimode GI optical fibers, the TD PFE is:

$$\frac{\partial P(m,\lambda,z,\omega)}{\partial z} + j\omega\tau(m,\lambda)P(m,\lambda,z,\omega) = -\alpha(m,\lambda)P(m,\lambda,z,\omega) + \frac{\partial P(m,\lambda,z,\omega)}{\partial m}\frac{\partial d(m,\lambda)}{\partial m} + d(m,\lambda)\frac{1}{m}\frac{\partial P(m,\lambda,z,\omega)}{\partial m} + d(m,\lambda)\frac{\partial P^2(m,\lambda,z,\omega)}{\partial m^2} \tag{2}$$

where $P(m,\lambda,z,\omega)$ is the power in the m - th principal mode (modal group) [32], z is position along the fiber axis from the input fiber end, $\alpha(m,\lambda)$ is the attenuation coefficient, $d(m,\lambda) \equiv D$ is the coupling coefficient, $\omega = 2\pi f$ is the baseband angular frequency, $\tau(m,\lambda)$ is delay time per unit length, which can be determined as:

$$\tau(m,\lambda) \cong \frac{n_1(\lambda)}{c}\left[1 + \frac{g-2}{g+2}\Delta(\lambda)\left(\frac{m}{M(\lambda)}\right)^{2g/(g+2)} + \frac{1}{2}\frac{3g-2}{g+2}\Delta(\lambda)^2\left(\frac{m}{M(\lambda)}\right)^{4g/(g+2)}\right] \tag{3}$$

where c is the free-space velocity of light and:

$$P(m,\lambda,z,\omega) = \int_{-\infty}^{+\infty} P(m,\lambda,z,t)\exp(-j\omega t)dt \tag{4}$$

The maximum principal mode number is [32]:

$$M(\lambda) = \sqrt{\frac{g\Delta(\lambda)}{g+2}}akn_1(\lambda) \tag{5}$$

where $k = 2\pi/\lambda$. Gaussian launch-beam distribution $P_0(\theta,\lambda,z=0)$ can be transformed into $P_0(m,\lambda,z=0)$ (one needs $P_0(m,\lambda,z=0)$ to numerically solve the TD PFE (2)), using the following relationship [32–34]:

$$\frac{m}{M} = \left[\left(\frac{\Delta r}{a}\right)^g + \frac{\theta^2}{2\Delta}\right]^{(g+2)/2g} \tag{6}$$

where Δr represents the radial separation (radial offset) between the launch beam point and the core center and θ represents the tilt angle measured in relation to the fiber axis. One should note that the condition of validity of the model proposed in this work is that guiding modes can be treated as a modal continuum. This is the case with all types of multimode optical fibers, such as a GI mPOF investigated in this work. Details regarding numerical solving the TD PFE (2) using EFDM and calculating bandwidth, can be found in our earlier work [35]. In this work, in order to further validate our proposed method for calculating bandwidth in a multimode GI mPOF, in our best knowledge for the first time, the TD PFE (2) is also solved using PINN. Methodology regarding numerical solving the partial differential equations (PDEs), such as TD PFE (2), using PINN are given in the Appendix A of this work.

We investigated the bandwidth in a multimode GI mPOF, which consists of different SI distributed layers (Fig. 1(b)), for which the effective V parameter is given as:

$$V = \frac{2\pi}{\lambda}a_{eff}\sqrt{n_{co}^2 - n_{fsm}^2} \tag{7}$$

where $a_{eff} = \Lambda/\sqrt{3}$ [40], and n_{fsm} is effective RI of different core and cladding layers, which can be obtained from equation (7), with the effective V parameter [40]:

$$V\left(\frac{\lambda}{\Lambda},\frac{d}{\Lambda}\right) = A_1 + \frac{A_2}{1 + A_3\exp(A_4\lambda/\Lambda)} \tag{8}$$

with the fitting parameters A_i ($i = 1$ to 4) given as:

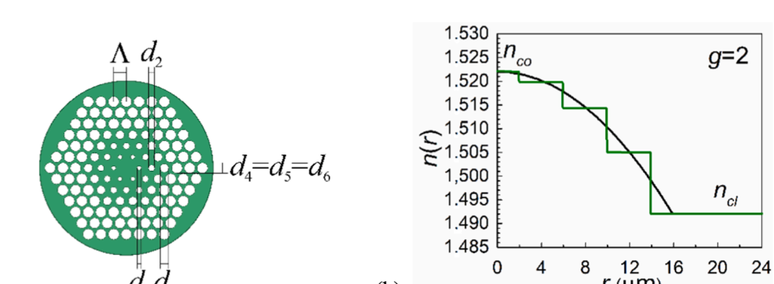

(a) (b)

Fig. 1. (a) The cross-section of the multimode GI mPOF (PMMA is the fiber material, shown in green color). A triangular lattice's air holes are positioned using pitch Λ. The air-hole sizes of the four inner air-hole rings in the core are d_1, d_2, d_3, and d_4. The cladding's air holes in rings 5 and 6 have the same diameter as those in air-hole ring 4 ($d_4 = d_5 = d_6$). (b) The referent multimode GI mPOF's RI performance (green solid line). The parabolic distribution of the RI in the core has $g = 2$ (black solid line). (For interpretation of the references to color in this figure legend, the reader is referred to the web version of this article.)

$$A_i = a_{i0} + a_{i1}\left(\frac{d}{\Lambda}\right)^{b_{i1}} + a_{i2}\left(\frac{d}{\Lambda}\right)^{b_{i2}} + a_{i3}\left(\frac{d}{\Lambda}\right)^{b_{i3}} \quad (9)$$

where the coefficients a_{i0} to a_{i3} and b_{i1} to b_{i3} ($i = 1$ to 4) are given in Table 1.

We applied our method to the multimode GI mPOF which has a core radius $a = 4\Lambda = 16\,\mu m$, where $\Lambda = 4\,\mu m$, and fiber diameter $b = 1$ mm. The GI mPOF material is PMMA, the same material as used for the GI POF (OM Giga, Fiber Fin^{TM}), which we previously investigated experimentally [35]. The RI of the core measured at the fiber axis is $n_{co} = 1.5220$ while the RI of the cladding is $n_{cl} = 1.4920$ [33,35,41]. For the GI mPOF under examination, the maximum principal mode number is $M = 24$ (the maximum mode number is $N = 580$) at $\lambda = 633$ nm, for $g = 2.0$ and $\Delta = (n_1 - n_2)/n_1 = 0.019711$.The modal attenuation is $\alpha(m,\lambda) \equiv \alpha_c = 0.0122\,\text{m}^{-1}$ and coupling coefficient is $D = 1482\,\text{m}^{-1}$ [35] (typical values of α_c and D for conventional multimode GI POFs and multimode GI mPOFs). The similar presumption was used to model a silica MOF [42]. For $\Lambda = 4\,\mu m$ and air-hole diameters of the four air-hole rings in the core $d_1 = 0.6\,\mu m$, $d_2 = 0.7\,\mu m$, $d_3 = 1.3\,\mu m$ and $d_4 = 3.1\,\mu m$, the RI $n_1 = 1.5201$, $n_2 = 1.5145$, $n_3 = 1.5050$ and $n_4 = 1.4920$, respectively, are calculated by means of equations (7) and (8). Thus, a parabolic RI distribution in the core with $g = 2.0$ is achieved (Fig. 1). The diameter of the cladding's air-holes in the rings 5 and 6 is $d_4 = d_5 = d_6 = 3.1\,\mu m$, which corresponds to the cladding RI $n_4 = n_5 = n_6 = n_{cl} = 1.4920$.

A Gaussian beam is assumed to be launched with $\langle\theta\rangle = 0^\circ$ in the numerical calculations. Fig. 2 shows the numerically estimated bandwidth using EFDM and PINN for four radial offsets $\Delta r = 0,\ 4,\ 8$ and $12\,\mu m$ for varied fiber lengths. A good agreement between solutions obtained using EFDM and PINN solutions can be seen. According to Fig. 2, bandwidth decreases as radial offset increases as a result of increased modal dispersion brought on by the excitation of higher guided modes. A more pronounced decline is seen with shorter fiber lengths. When the fiber length is $z \approx 20$ m, which is close to the theoretically determined coupling length $L_c = 18$ m [37] at which an EMD is established, strong mode coupling results in bandwidth improvement (slower bandwidth drop) in multimode GI mPOFs. An SSD is established as fiber length increases (in our earlier work [41], we found that an SSD is established at $z = 60$ m). As fiber length further increases, bandwidth becomes essentially radially offset-independent. Consequently, assuming a radial offset of $\Delta r = 0\,\mu m$ for the examined GI mPOF, we obtain a bandwidth of around 28 GHz at a distance of 100 m, which results in a bandwidth-length product of 2.8 GHz·km. This bandwidth-length product is substantially higher than those for standard GI POFs studied in our earlier work [35] (Fig. 3) and Chun-Yu Lin et al.'s work [43], which were 0.46 GHz·km and 0.156 GHz·km, respectively. Because the GI mPOF investigated in this work has a smaller core radius and fewer propagating modes than a conventional GI POF, the EMD is obtained in GI mPOF at a shorter length. Namely, the coupling length of $L_c = 31$ m is reported for conventional GI POF [33]. When there are fewer propagating modes, the mode coupling process requires a shorter length to complete, accelerating the transition to the slower bandwidth drop phase. The mode coupling process requires a shorter length to complete the mode coupling process when there are fewer propagating modes, which accelerates the transition to the slower bandwidth decline regime.

Table 1
The fitting coefficients in equation (9).

	$i = 1$	$i = 2$	$i = 3$	$i = 4$
a_{i0}	0.54808	0.71041	0.16904	−1.52736
a_{i1}	5.00401	9.73491	1.85765	1.06745
a_{i2}	−10.43248	47.41496	18.96849	1.93229
a_{i3}	8.22992	−437.50962	−42.4318	3.89
b_{i1}	5	1.8	1.7	−0.84
b_{i2}	7	7.32	10	1.02
b_{i3}	9	22.8	14	13.4

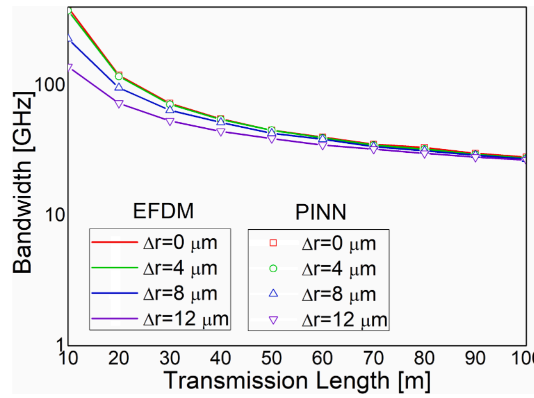

Fig. 2. Numerically calculated bandwidth using EFDM (lines) and PINN (open symbols) as a function of transmission length of GI mPOF for various radial offsets.

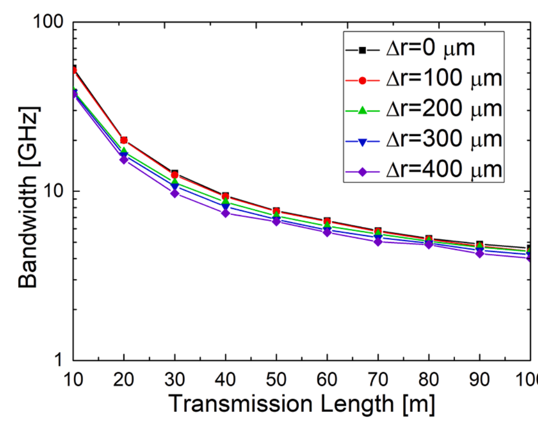

Fig. 3. Measured bandwidth (solid symbols) as a function of transmission length of conventional multimode GI POF for various radial offsets (lines are drawn to guide the eye) [35].

Improved fiber performance on GI mPOF lines, especially in in-home networks, can be attained by using such a fiber characterization. This optimization can be carried out by comparing the performance characteristics and numerical simulation results of different GI mPOFs with different RI distribution (different g), coupling coefficient D, and attenuation α_c. Finally, since in contrast to GI POF, fabrication of GI mPOF does not require an advanced doping techniques and, as shown in this work, and it can achieve a much higher bandwidth, it deserves recommendation as a good choice for various high bandwidth fiber optic systems. A range of different fabrication methods is available for mPOF preform fabrication, including extrusion, drilling, casting or injection molding [7,44].

Conclusion

By numerically solving the TD PFE using the EFDM and PINN, we were able to determine the bandwidth for various multimode GI mPOF launch conditions (radial offsets). We discovered that when radial offset increases, bandwidth decreases. There is a more noticeable bandwidth decrease at short fiber lengths. The fact that this decline slows down as coupling length L_c gets closer to the point at which an EMD is reached, shows how strongly mode coupling affects the bandwidth in GI mPOFs. The length at which EMD is reached is shorter, the quicker the bandwidth would change from a steep to a moderate bandwidth decrease. The formation of an SSD is indicated by the bandwidth becoming almost entirely independent of radial offset as fiber length is extended. Consequently, for the GI mPOF that was the subject of this work, with radial offset of $\Delta r = 0\,\mu m$, we obtain a bandwidth-length product of 2.8 GHz·km. This bandwidth-length product is substantially higher than those for typical GI POFs studied in our previous work [35] and Chun-Yu Lin et al.'s work [43], which were 0.46 GHz·km and 0.156 GHz·km, respectively. We have demonstrated that GI mPOF has a wider bandwidth compared to its conventional counterpart due to carefully tuned structure of the GI mPOF, which allowed reduction of modal dispersion-induced pulse spreading. Furthermore, mPOFs with a relatively large core diameter can support multiple modes, which can be used for mode-division multiplexing to increase the bandwidth.

Funding

This research was funded by the National Natural Science Foundation of China (62111530238, 62003046); the Strategic Research Grant of City University of Hong Kong (Project No. CityU 7004600); The grants from Serbian Ministry of Science, Technological Development and Innovations (Agreement No. 451–03-68/2022–14/200122 and 451–03-47/2023–01/200123); The grant from Science Fund of the Republic of Serbia (Agreement No. CTPCF-6379382); Guangdong Basic and Applied Basic Research Foundation (2021A1515011997); Special project in key field of Guangdong Provincial Department of Education (2021ZDZX1050); The Innovation Team Project of Guangdong Provincial Department of Education (2021KCXTD014); Department of Science and Technology of Guangdong Province (2021A1313030055).

Declaration of Competing Interest

The authors declare that they have no known competing financial interests or personal relationships that could have appeared to influence the work reported in this paper.

Data availability

Data will be made available on request.

Appendix A. : PINN for solving PDEs

The PINN is a machine-learning technique that can be used to approximate the solution of PDEs. PDEs with corresponding initial and boundary conditions can be expressed in a general form as [45]:

$$\begin{aligned} &\frac{\partial u(x,t)}{\partial t} + \mathrm{N}[u(x,t)] = 0, \quad x \in \Omega, \quad t \in [0,T] \\ &u(x,t=0) = h(x), \quad x \in \Omega \\ &u(x,t) = g(x,t), \quad x \in \Omega_g, \quad t \in [0,T] \end{aligned} \tag{A1}$$

Here, N is a differential operator, $x \in \Omega \subseteq R^d$ and $t \in R$ represent spatial and temporal dimensions respectively, $\Omega \subseteq R^d$ is a computational domain, $\Omega_g \subseteq \Omega$ is a computational domain of the exposed boundary conditions, $u(x,t)$ is the solution of the PDEs with initial condition $h(x)$ and boundary conditions $g(x,t)$.

PINN consists of two subnets: an approximator network and a residual network. The approximator network receives input $u(x,t)$ undergoes the training process, and provides an approximate solution $\widehat{u}(x,t)$ as an output. The approximator network trains on a grid of points, called collocation points, sampled randomly or regularly from the simulation domain. The weights and biases of the approximator network make up a set of trainable parameters, trained by minimizing a composite loss function of the following form:

$$L = L_r + L_0 + L_b \tag{A2}$$

where:

$$\begin{aligned} &L_r = \frac{1}{N_r}\sum_{i=1}^{N_r} \left|u\left(x^i,t^i\right) + N\left[u\left(x^i,t^i\right)\right]\right|^2 \\ &L_0 = \frac{1}{N_0}\sum_{i=1}^{N_0} \left|u\left(x^i,t^i\right) - h^i)\right|^2 \\ &L_b = \frac{1}{N_b}\sum_{i=1}^{N_b} \left|u\left(x^i,t^i\right) - g^i)\right|^2 \end{aligned} \tag{A3}$$

Here, L_r, L_0, and L_b represent residuals of governing equations, initial and boundary conditions, respectively. N_r, N_0, and N_b are the numbers of mentioned collocation points of the computational domain, initial and boundary conditions, respectively. These residuals are computed by a non-trainable part of the PINN model called the residual network. The approximator network is used to approximate the solution $u(x,t)$ which then goes to the residual network to calculate the residual loss L_r, boundary condition loss L_b, and initial condition loss L_0. The weights and biases of the approximator network are trained using a composite loss function consisting of residuals L_r, L_0, and L_b through gradient-descent technique based on the back-propagation [45]. To calculate the residual L_r, PINN requires derivatives of the outputs with respect to the inputs x and t. Such calculation is done through automated differentiation, which relies on the fact that combining derivatives of the constituent operations by the chain rule produces the derivative of the entire composition.

References

[1] Barbio C, Mekonnen KA, Huijskens F, Koonen T, Tangdiongga E. Bidirectional gigabits per second spatial diversity link using POF for passive optical front-ends. J Light Technol 2022;40(20):6753–61.
[2] Huang O, Shi J, Chi N. Performance and complexity study of a neural network post-equalizer in a 638-nm laser transmission system through over 100-m plastic optical fiber. Opt Eng 2022;61(12):126108.
[3] Ye Y, Zhao C, Wang Z, Teng C, Marques C, Min R. Portable multi-hole plastic optical fiber sensor for liquid level and refractive index monitoring. IEEE Sens J 2023;23(3):2161–8.

[4] Teng C, Wang Y, Min R, Deng S, Deng H, Li Y, et al. Plastic optical fiber based SPR sensor for simultaneous measurement of refractive index and liquid level. IEEE Sens J 2022;22(7):6677–84.
[5] Leal-Junior A, Guo J, Min R, Fernandes AJ, Frizera A, Marques C. Photonic smart bandage for wound healing assessment. Photonics Res 2021;9(3):272–80.
[6] Guo J, Niu M, Yang C. Highly flexible and stretchable optical strain sensing for human motion detection. Optica 2017;4(10):1285–8.
[7] Fasano A, Woyessa G, Stajanca P, Markos C, Stefani A, Nielsen K, et al. Fabrication and characterization of polycarbonate microstructured polymer optical fibers for high-temperature-resistant fiber Bragg grating strain sensors. Opt Mater Express 2016;6(2):649–59.
[8] Zubel MG, Fasano A, Woyessa GT, Min R, Leal AG, Theodosiou A, et al. Bragg gratings inscribed in solid-core microstructured single-mode polymer optical fiber drawn from a 3D-printed polycarbonate preform. IEEE Sens J 2020;20(21):12744–57.
[9] Akimoto Y, Asai M, Koike K, Makino K, Koike Y. Poly(styrene)-based graded-index plastic optical fiber for home networks. Opt Lett 2012;37(11):1853–5.
[10] Makino K, Akimoto Y, Koike K, Kondo A, Inoue A, Koike Y. Low loss and high bandwidth polystyrene-based graded index polymer optical fiber. J Light Technol 2013;31(14):2407–12.
[11] Leal-Junior AG, Theodosiou A, Min R, Casas J, Díaz CR, Dos Santos WM, et al. Quasi-distributed torque and displacement sensing on a series elastic actuator's spring using FBG arrays inscribed in CYTOP fibers. IEEE Sens J 2019;19(11):4054–61.
[12] Chapalo I, Chah K, Gusarov A, Ioannou A, Pospori A, Nan Y-G, et al. Gamma-radiation enhancement of sensing properties of FBGs in a few-mode polymer CYTOP fiber. Opt Lett 2023;23(1):39.
[13] Woyessa G, Rasmussen HK, Bang O. Zeonex – a route towards low loss humidity insensitive single-mode step-index polymer optical fibre. Opt Fiber Technol 2020;57:1–6.
[14] Dash JN, Cheng X, Tam H. Low gas pressure sensor based on a polymer optical fiber grating. Opt Lett 2021;46(5):933–6.
[15] Markos C, Stefani A, Nielsen K, Rasmussen HK, Yuan W, Bang O. High-Tg TOPAS microstructured polymer optical fiber for fiber Bragg grating strain sensing at 110 degrees. Opt Express 2013;21(4):4758–65.
[16] Woyessa G, Fasano A, Stefani A, Markos C, Nielsen K, Rasmussen HK, et al. Single mode step-index polymer optical fiber for humidity insensitive high temperature fiber Bragg grating sensors. Opt Express 2016;24(2):1253–60.
[17] Broadway C, Min R, Leal-Junior AG, Marques C, Caucheteur C. Toward commercial polymer fiber Bragg grating sensors: Review and applications. J Light Technol 2019;37(11):2605–15.
[18] Cheng X, Gunawardena DS, Pun CJ, Bonefacino J, Tam H. Single nanosecond-pulse production of polymeric fiber Bragg gratings for biomedical applications. Opt Express 2020;28(22):33573–83.
[19] Kuang R, Ye Y, Chen Z, He R, Savović I, Djordjevich A, et al. Min Low-cost plastic optical fiber integrated with smartphone for human physiological monitoring. Opt Fiber Technol 2022;71:102947.
[20] X. Hu, Z. Chen, X. Cheng, Min, H. Qu, C. Caucheteur, and H.-Y. Tam, Femtosecond laser point-by-point Bragg grating inscription in BDK-doped step-index PMMA optical fibers, *Opt. Lett.* 47(2), 249-252 (2022).
[21] Theodosiou A, Min R, Leal-Junior AG, Ioannou A, Frizera A, Pontes MJ, et al. Long period grating in a multimode cyclic transparent optical polymer fiber inscribed using a femtosecond laser. Opt Lett 2019;44(21):5346–9.
[22] Knight JC, Birks TA, St P, Russell J, Atkin DM. All-silica single-mode optical fiber with photonic crystal cladding. Opt Lett 1996;21(19).
[23] K. Stefańska, S. Majchrowska, K. Gemza, G. Soboń, J. Sotor, P. Mergo, K. Tarnowski, and T. Martynkien, Soliton trapping and orthogonal Raman scattering in a birefringent photonic crystal fiber, *Opt. Lett.* 47(16), 4183-4186 (2022).
[24] Zhao S, Guo R, Zeng Y. Effects of frequency-dependent Kerr nonlinearity on higher-order soliton evolution in a photonic crystal fiber with one zero-dispersion wavelength. Phys Rev A 2022;106(3):033516.
[25] Wang C, Lin K, Cao S, Feng G, Wang J, Abdalla AN. Polarized supercontinuum generation in CS 2-core all-normal dispersion photonic crystal fiber. IEEE Photon J 2022;14(6):1–7.
[26] Heydarian K, Nosratpour A, Razaghi M. Computational study of wavelength conversion based on XGM by photonic crystal semiconductor optical amplifier. Opt Laser Technol 2022;156(1):108531.
[27] Eijkelenborg MA, Large MCJ, Argyros A, Zagari J, Manos S, Issa NA, et al. Microstructured polymer optical fibre. Opt Express 2001;9(7):319–27.
[28] Woyessa G, Pedersen JKM, Fasano A, Nielsen K, Markos C, Rasmussen HK, et al. Zeonex-PMMA microstructured polymer optical FBGs for simultaneous humidity and temperature sensing. Opt Lett 2017;42(6):1161–4.
[29] Min R, Pereira L, Paixao T, Woyessa G, Hu X, Antunes P, et al. Chirped POF Bragg grating production utilizing UV cure adhesive coating for multiparameter sensing. Opt Fiber Technol 2021;65:102593.
[30] Lwin R, Barton G, Harvey L, Harvey J, Hirst D, Manos S, et al. Beyond the bandwidth-length product: Graded index microstructured polymer optical fiber. Appl Phys Lett 2007;91(19):191119.
[31] Garito AF, Wang J, Gao R. Effects of random perturbations in plastic optical fibers. Science 1998;281:962–7.
[32] Olshansky R. Mode coupling effects in graded-index optical fibers. Appl Opt 1975;14:935–45.
[33] Savović S, Simović A, Drljača B, Djordjevich A, Stepniak G, Bunge CA, et al. Power flow in graded index plastic optical fibers. J Lightwave Technol 2019;37:4985–90.
[34] Nagano K, Kawakami S. Measurements of mode conversion coefficients in graded-index fibers. Appl Opt 1980;19:2426–34.
[35] A. Simović, A. Djordjevich, B. Drljača, S. Savović, and R. Min, Investigation of bandwidth in multimode graded index plastic optical fibers, *Opt. Express* 29, 29587-29594 (2021).
[36] Dadabayev R, Malka D. A visible light RGB wavelength demultiplexer based on polycarbonate multicore polymer optical fiber. Opt Laser Technol 2019;116:239–45.
[37] Gelkop B, Aichnboim L, Malka D. RGB wavelength multiplexer based on polycarbonate multicore polymer optical fiber. Opt Fiber Technol 2021;61:102441.
[38] Malka D, Peled A. Power splitting of 1×16 in multicore photonic crystal fibers. Appl Surface Sci 2017;417:34–9.
[39] Malka D, Cohen E, Zalevsky Z. Design of 4×1 power beam combiner based on multicore photonic crystal fiber. Appl Sci 2017;7:695.
[40] Saitoh K, Koshiba M. Empirical relations for simple design of photonic crystal fibers. Opt Express 2005;13(1):267–74.
[41] S. Savović, A. Simović, B. Drljača, M. S. Kovačević, Lj. Kuzmanović, A. Djordjevich, K. Aidinis, and R. Min, Power flow in multimode graded-index microstructured polymer optical fibers, *Polymers* 15, 1474 (2023).
[42] Savović S, Kovačević MS, Simović A, Kuzmanović L, Drljača B, Djordjevich A. Method for investigation of mode coupling in multimode step-index silica photonic crystal fibers. Optik 2021;246:167728.
[43] Lin C-Y, Li C-Y, Lu H-H, Chang C-H, Peng P-C, Lin C-R, Chen J-H. A hybrid CATV/16-QAM-OFDM in-house network over SMF and GI-POF/VLC transport. IEEE Phot Technol Lett 2015;27:526–9.
[44] van Eijkelenborg MA, Large MCJ, Argyros A, Zagari J, Manos S, Issa NA, et al. Microstructured polymer optical fibre. Opt Express 2001;9:319–27.
[45] Raissi M, Perdikaris P, Karniadakis GE. Physics-informed neural networks: A deep learning framework for solving forward and inverse problems involving nonlinear partial differential equations. J Computat Phys 2019;378:686–707.